Corrosion Science 237 (2024) 112329

Contents lists available at ScienceDirect

Corrosion Science

journal homepage: www.elsevier.com/locate/corsci

Effect of reactive elements in MCrAlX bond coat for durability improvement of thermal barrier coatings

Masahiro Negami [a,b,*], Ryo Morihashi [b], Tessei Yoshino [a], Ryoji Sahara [c], Yoko Yamabe-Mitarai [a]

[a] Department of Advanced Materials Science, Graduate School of Frontier Sciences, The University of Tokyo, Kashiwanoha 5-1-5, Kashiwa-shi, Chiba 277-8561, Japan
[b] Kawasaki Heavy Industries, Ltd., Kawasaki-cho 1-1, Akashi-shi, Hyogo 673-8666, Japan
[c] Research Center for Structural Materials, National Institute for Materials Science, Sengen 1-2-1, Tsukuba-shi, Ibaraki 305-0047, Japan

ARTICLE INFO

Keywords:
Thermal barrier coatings
High temperature oxidation
Thermally grown oxide
Reactive elements
First principles calculation

ABSTRACT

The effects of reactive elements (RE) in MCrAlX alloy (M: Metals, X: RE) as the bond coat for thermal barrier coatings durability were investigated by both experimental evaluation and density functional theory (DFT) calculations. Cyclic oxidation tests showed that the lifetime of the sample with Y, Hf, and Si as RE displayed approximately twice of the sample with Y only. Furthermore, the interface energies between oxide (α-Al_2O_3) and bond coat with various RE (Si, Sc, Ti, Y, Zr, Hf, La, and Ce) were calculated by DFT. DFT results indicate that Hf and Si doping effectively reduce the interface energy.

1. Introduction

Thermal barrier coatings (TBC) are applied to high-temperature components of gas turbines to protect the metal components from combustion gases [1–7]. TBC have become an indispensable technology for aero engines as well as for industrial gas turbines used for power generation. Recently, social demands to reduce carbon emissions have caused increased demands for improving power generation efficiency, and the turbine inlet temperature (TIT) of the industrial gas turbine has been markedly increased. In addition, with the increase of renewable energy share, gas turbines are required to operate to fill in gaps between demands and renewable energy power output, which is inherently unstable. As a result, the frequency of starts and stops in operation is anticipated to rise. Such an increase in TIT and thermal cycles should have a negative impact on TBC durability; however, current TBC does not have sufficient durability to satisfy these operational requirements.

Generally, TBC consists of two layers: a top coat and a bond coat [1]. The top coat is a thermal barrier layer and usually consists of yttria stabilized zirconia (YSZ) [8], which has a high coefficient of thermal expansion and low thermal conductivity. The bond coat provides oxidation resistance and adhesion with the top coat [1,9]. MCrAlX alloys are commonly used as the bond coat. M presents a base metal composition, such as Ni, Co, or both. X is called “Reactive elements (REs)”, including Y, Hf, Si, etc, and is added to improve the oxidation resistance [10]. The bond coat is deposited by thermal spray using low-pressure plasma spray (LPPS) or high-velocity oxi-fuel (HVOF) process.

Although various factors have possibilities to cause damage to TBC [11,12], the oxidation of the bond coat is considered the major issue that ultimately limits the lifetime of the TBC. Because the top coat of YSZ, which is a well-known good oxygen ion conductor, cannot avoid high-temperature oxidation of the bond coat, thermally grown oxide (TGO) is formed at the interface between the top coat and the bond coat. Because TGO, which consists of α-Al_2O_3, has a lower coefficient of thermal expansion than the bond coat and the top coat [13], the mismatch of thermal expansion causes thermal stress during thermal cycling [3]. Cracks at the interface between the TGO and the bond coat is generated owing to thermal stress. Such clacks or micro spallation of the TGO from the bond coat will propagate to the surrounding area and finally reach complete spalling of the top coat[2].

Considering this spalling mechanism of TBC, the lifetime of TBC will be increased if the adhesion of the TGO to the bond coat is improved by modifying the bond coat composition. RE are known to be effective in improving the adhesion of TGO [14], and if the composition of RE addition can be optimized, the durability of TBC will be improved. In particular, several previous studies have investigated the durability of TBC with MCrAlX bond coat with different species of RE doping [15–17]. For example, Haynes et al. evaluated TBC with bond coat of different RE addition (Y only or YHfSi) by cyclic oxidation test, and

* Corresponding author at: Kawasaki Heavy Industries, Ltd., Kawasaki-cho 1-1, Akashi-shi, Hyogo 673-8666, Japan.
E-mail address: masahiro_negami@global.kawasaki.com (M. Negami).

https://doi.org/10.1016/j.corsci.2024.112329
Received 23 April 2024; Received in revised form 30 June 2024; Accepted 28 July 2024
Available online 2 August 2024

Table 1
Chemical composition of Ni-base superalloy used for substrates and MCrAlX used for bond coat of TBC samples (wt%).

	Cr	Ni	Co	Mo	W	Ta	Ti	Al	Y	Si	Hf	Re
CMSX−4	6.5	Bal.	9	0.6	6	6.5	1	5.6	-	-	0.1	3
NiCoCrAlY	17	Bal.	23	-	-	-	-	13	0.45	-	-	-
NiCoCrAlYHfSi	17	Bal.	22	-	-	-	-	12	0.5	0.4	0.45	-

reported that TBC with YHfSi bond coat displayed approximately 20 ~ 40 % better cycle life [15]. However, the crack propagation process to TBC spalling was not analyzed in detail in their study, and it is unclear how the additional doping of Hf and Si affected the lifetime of the TBC.

Moreover, there is controversy about the mechanism by which the REs improve the adhesion of the TGO [10]. It has been almost 80 years since the publication of the patent on the effect of RE on oxidation resistance [18,19], and the studies on the effects of RE have been published [10,14,20]. Several mechanisms were proposed to explain adhesion improvements. Oxide pegging is a known mechanism, in which particles of RE oxides called "peg" at the interface improve adhesion owing to their anchoring effect [21]. Sulfur gettering is another mechanism in which RE traps impurity sulfur, which segregates to the interface and causes deterioration of interfacial adhesion [22,23]. These mechanisms have been experimentally confirmed and are widely accepted. However, these mechanisms are indirect mechanisms of improving the adhesion of TGO. Although it has been observed that RE segregates at the interface between the alloy and TGO [24–26], the effect of segregated RE on the adhesion strength is not fully understood. In addition, conventional mechanisms do not sufficiently explain the difference in quantitative adhesion strength depending on the RE composition.

Recently, several attempts have been made to reveal the atomic-scale effect of doped RE for the scale-alloy interface by first-principles calculations based on density functional theory (DFT) [27–32]. For example, Jiang et al. evaluated the effect of Hf addition to α-Al_2O_3/Ni interface and reported that the addition of Hf increases the work of separation. This result provides evidence for improved adhesion by Hf-doping. Moreover, they showed that the presence of sulfur decreases the work of separation [29]. However, the differences in the effects of various RE, their systematic understanding, and the origin of the adhesion improvement have not been fully elucidated.

Our final goal is to improve the durability of TBC by optimizing the RE of MCrAlX used as the bond coat. The first step toward this goal, we aimed to clarify the effect of RE doping from both experimental and computational approaches in this study.

First, as an experimental approach, we prepared TBC samples with bond coats of two different RE doping (Y only or YHfSi) and compared their durability as the cyclic oxidation test, and attempted to clarify how the RE doping contributes to the improvement in durability by observing the damage processes.

Moreover, DFT calculations were performed to reveal the adhesion enhancement effect of various RE, such as Si, Sc, Ti, Y, Zr, La, Ce, and Hf, on the interface between γ-Ni and α-Al_2O_3. We verified whether the experimental results could be explained by theoretical calculations, and clarified the origin and trend of the adhesion improvement by RE doping.

2. Experimental methods

2.1. Samples

A Ni-based superalloy (CMSX-4) was used as substrates. NiCoCrAlY alloy or NiCoCrAlYHfSi alloy was thermally sprayed onto the substrates using HVOF method as the bond coat. The chemical composition of each alloy is shown in Table 1. After applying the bond coat, pre-oxidation heat treatment was performed under the conditions described in our previous report (under vacuum atmosphere conditions (PO_2 = approx. 10^{-14} Pa) at 1080°C for 4 hours) [33]. Subsequently, 8 wt% yttria-stabilized zirconia (8YSZ) powder was thermally sprayed as the top coat using atmospheric plasma spray (APS) methods. The sample size was 20 × 20 × 5 mm^3.

2.2. Cyclic oxidation test

Cyclic oxidation tests were conducted to evaluate the durability of TBC samples. These tests were based on ISO 14188:2012 (E) [34]. An atmospheric furnace equipped with an automatic sample loading and unloading mechanism was used. For cyclic tests, the samples were maintained at 1100°C for 30 min in the furnace and cooled outside the furnace for 10 mins for each cycle. During cooling, the samples were forced to cool in the air by a fan. The damage of the samples was examined every 25 cycles, and the number of cycles to failure was defined as the cycles at which TBC has spalled more than 30 % of the surface area.

Seven specimens were tested for each sample type (NiCoCrAlY of NiCoCrAlYHfSi), and four of them were removed at 50, 100, 200, and 400 cycles for cross-sectional observation. The remaining three specimens were tested until spalling.

The surface roughness of the bond coat was measured with a laser microscope (VK-260, Keyence). This measurement was performed on the bond coat sample prepared under the same process conditions as the TBC samples.

Cross-sectional observation of the samples before and after the cyclic oxidation tests was performed using a scanning electron microscope (SEM, SU5000, Hitachi). The composition maps of the bond coat were investigated using energy-dispersive X-ray spectroscopy (EDX, Octane Elect Plus, EDAX) after polishing by ion milling.

The TGO thickness was measured from cross-sectional backscattered electron (BSE) images using the following method: Three images with 130 μm (after 50, 100, and 200 cycles) or 350 μm (after 400 cycles) were taken for each oxidation condition, and then a TGO thickness of five points with equal spacing was measured. The TGO thickness was determined for each sample by averaging the thickness values obtained at 15 observed points.

The detailed microstructure between the TGO and bond coat was characterized using a scanning transmission electron microscope (STEM, Talos F200X, FEI) operated at 200 kV equipped with an energy dispersive X-ray (EDX) analyzer. Cross-sectional TEM specimens were prepared using focused ion beam (FIB) thinning.

3. Theoretical methods

First-principles calculations were performed using the Quantum ESPRESSO software, which is the plane wave-based implementation of DFT [35]. We employed the projector augmented wave (PAW) method [36] to represent the interactions between electrons and ions while the exchange correlation was described using the Perdew–Burke–Ernzerhof (PBE) parametrization of the generalized gradient approximation (GGA) [37].

Because the MCrAlX coating has the two-phase structure consisting of γ-Ni phase and β-NiAl phase, both α-Al_2O_3/γ-Ni interface and α-Al_2O_3/β-NiAl seem to be candidates for the calculation to evaluate the interface between the TGO and the bond coat. However, after relatively short-time exposure in high-temperature environment, the microstructure of the bond coat near the TGO changes to only γ-Ni phase because of

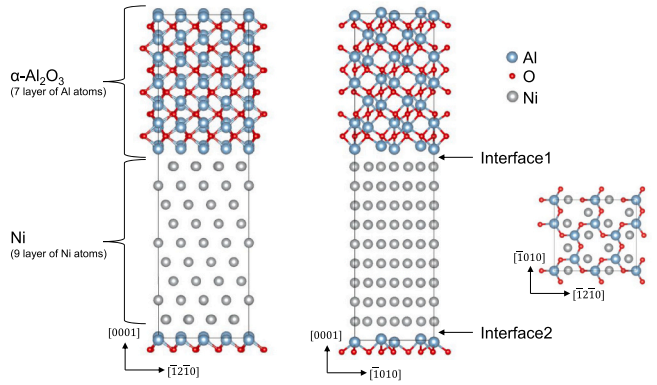

Fig. 1. Interface model of α-Al_2O_3(0001) / γ-Ni(111) with 236 atoms.

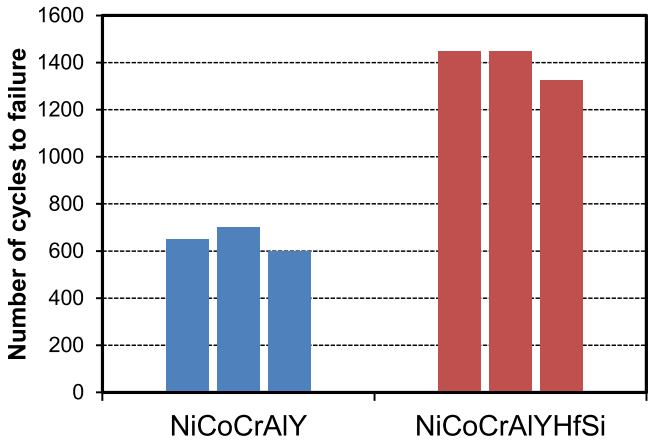

Fig. 2. Cycles to failure of TBC samples during cyclic oxidation tests of 30 min cycles at 1100℃.

Al depletion for forming TGO. Our previous study revealed that the β-NiAl has already disappeared from the interface in contact with TGO only after 50 h oxidation at 1050℃ [38]. Therefore, we targeted the α-Al_2O_3/γ-Ni interface for the DFT calculations.

To evaluate the adhesion strength between α-Al_2O_3 and γ-Ni interface, we used the model shown in Fig. 1. In this model, the Al-terminated α-Al_2O_3(0001) and γ-Ni(111) are in contact at two interfaces. The α-Al_2O_3(0001) plane was selected due to its preferential orientation on MCrAlY surface [39]. γ-Ni(111) was selected due to its structural similarity to α-Al_2O_3(0001). $<110>_{\gamma\text{-Ni}}$ is parallel to $<\bar{1}2\bar{1}0>_{\alpha\text{-Al2O3}}$. γ-Ni consists of nine layers, and each layer has 12 Ni atoms. α-Al_2O_3 consists of seven layers of Al, and each layer has eight Al atoms. This model consists of 236 atoms.

Although the O-terminated structure seems to be another possibility, we selected the Al-terminated structure for the following reason. We conducted preliminary calculations for both the Al-terminated and the O-terminated structure, and confirmed that the interface energy of the O-terminated structure was larger and more unstable than that of the Al-terminated structure. It is consistent with the results of Jarvis et al. [40].

The in-plane lattice mismatch between α-Al_2O_3(0001) and γ-Ni(111) is approximately 9 %, with γ-Ni under tensile, and the gap between α-Al_2O_3(0001) and γ-Ni(111) was initially set to 1.5 Å. The interface area is approximately 74 $Å^2$.

Brillouin zone integrations were performed using a set of 2×2×1 k-points for this 236 atoms model (Fig. 1). The cut-off energy for the plane wave expansion was set at 50 Ry. Gaussian smearing was used for the energy calculation with a smearing width of 0.01 Ry. The total energy was minimized over the degrees of freedom of the electron density and the ionic positions and structural parameters. Convergence threshold for energy and atomic forces was set to 10^{-6} Ry and 10^{-3} Ry/bohr, respectively.

By employing the above parameters, we performed structural relaxation calculation for a 108-atom model of γ-Ni (only the Ni part of the interface model with 236 atoms, shown in Fig. S1), and the lattice parameter (3.51 Å) was in good agreement with the experimental value (3.52 Å) [41] within 1 %. Structural relaxation calculations for a 120-atom model of α-Al_2O_3 (only the α-Al_2O_3 part of the interface model with 236 atoms, shown in Fig. S2) was also performed, and the lattice parameter (a, b = 4.83 Å, c = 13.18 Å) was in good agreement with the experimental value (a, b = 4.76 Å, c = 12.98 Å)[42] within 2 %.

Structural relaxation calculations were performed for all atomic positions to obtain the ideal stable interface structure. Subsequently, the relaxed structures were used for the calculation of interface energy.

To understand the adhesion strength of the interface between α-Al_2O_3(0001) and γ-Ni(111), we calculated the interface energy (γ_{clean}), which is expressed as

$$\gamma_{clean} = \frac{E_{system\ with\ interface} - E_{system\ without\ interface}}{2A} \quad (1)$$

Here, A is the area of the interface, $E_{system\ with\ interface}$ is the total energy of the interface model. Because of the three-dimensional periodic boundary conditions, two interfaces were introduced in the model (shown in Fig. 1), and γ_{clean} was divided by two, as shown in Eq. (1). In the present model, $E_{system\ without\ interface}$ is expressed as

$$E_{system\ without\ interface} = E_{Al_2O_3} + E_{Ni} + E_{Al} \quad (2)$$

$E_{Al_2O_3}$, E_{Ni}, and E_{Al} are the energies of α-Al_2O_3 with 24 formula units, γ-Ni with108 atoms, and metallic Al with 8 atoms. E_{Al} was introduced to correct energy because the Al-terminated model of Fig. 1 has more eight Al atoms than the stoichiometric composition of α-Al_2O_3.

For the calculation of the RE doped model, we first determined the favorable position for doped RE in the interface model. For this calculation, we used a 118-atoms model (Fig. S3) that was halved in length for $[\bar{1}2\bar{1}0]$ direction from the model shown in Fig. 1. Brillouin zone integrations were changed to use a set of 2×3×1 k-points for 118-atoms model (Fig. S3).

We calculated the interface energy of the RE-doped model in which one Al atom was replaced for RE atom at the most favorable site. For this calculation, full-sized 236-atoms model (Fig. 1) was used. The interface energy γ_{RE} of the RE-doped model is expressed as,

$$\gamma_{RE} = \frac{E_{system\ with\ interface+RE} - E_{system\ witout\ interface+RE} - A\gamma_{clean}}{A} \quad (3)$$

$E_{system\ with\ interface+RE}$ is the total energy of RE-doped interface model. $E_{system\ without\ interface+RE}$ is expressed as

$$E_{system\ without\ interface+RE} = E_{Al_2O_3+RE} + E_{Ni} + E_{Al} \quad (4)$$

$E_{Al_2O_3+RE}$ is the total energy of α-Al_2O_3 model with 24 formula units in which one Al atom was replaced for RE.

To understand the chemical bonding of each atom at the interface, the charge density (*CD*) and the charge density difference (*CDD*) were calculated as follows:

$$CDD = CD_{system\ with\ interface+RE} - \left(CD_{system\ with\ interface-RE} + CD_{RE}\right) \quad (5)$$

Here, $CD_{system\ with\ interface+RE}$ is the charge density of the interface model with doped-RE, $CD_{system\ with\ interface-RE}$ is the charge density of the interface model excluding only doped-RE atoms without changing each atom coordinate, and CD_{RE} is the charge density of the isolated single RE atom.

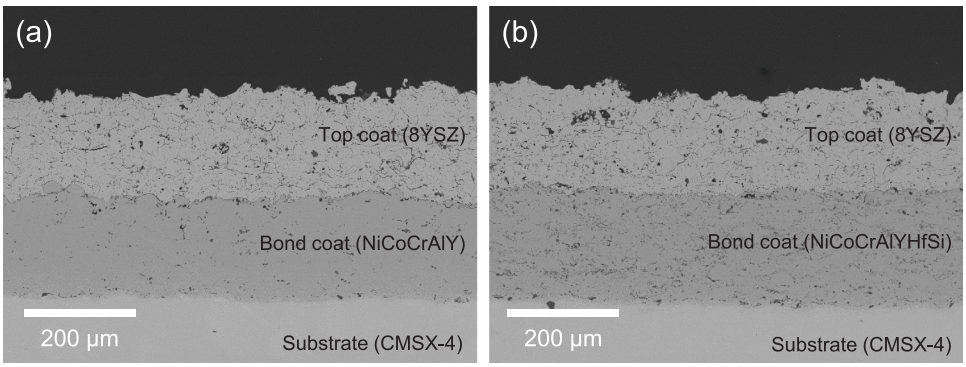

Fig. 3. Cross-section SEM-BSE images of TBC samples before cyclic oxidation tests. (a) NiCoCrAlY bond coat sample, (b) NiCoCrAlYHfSi bond coat sample.

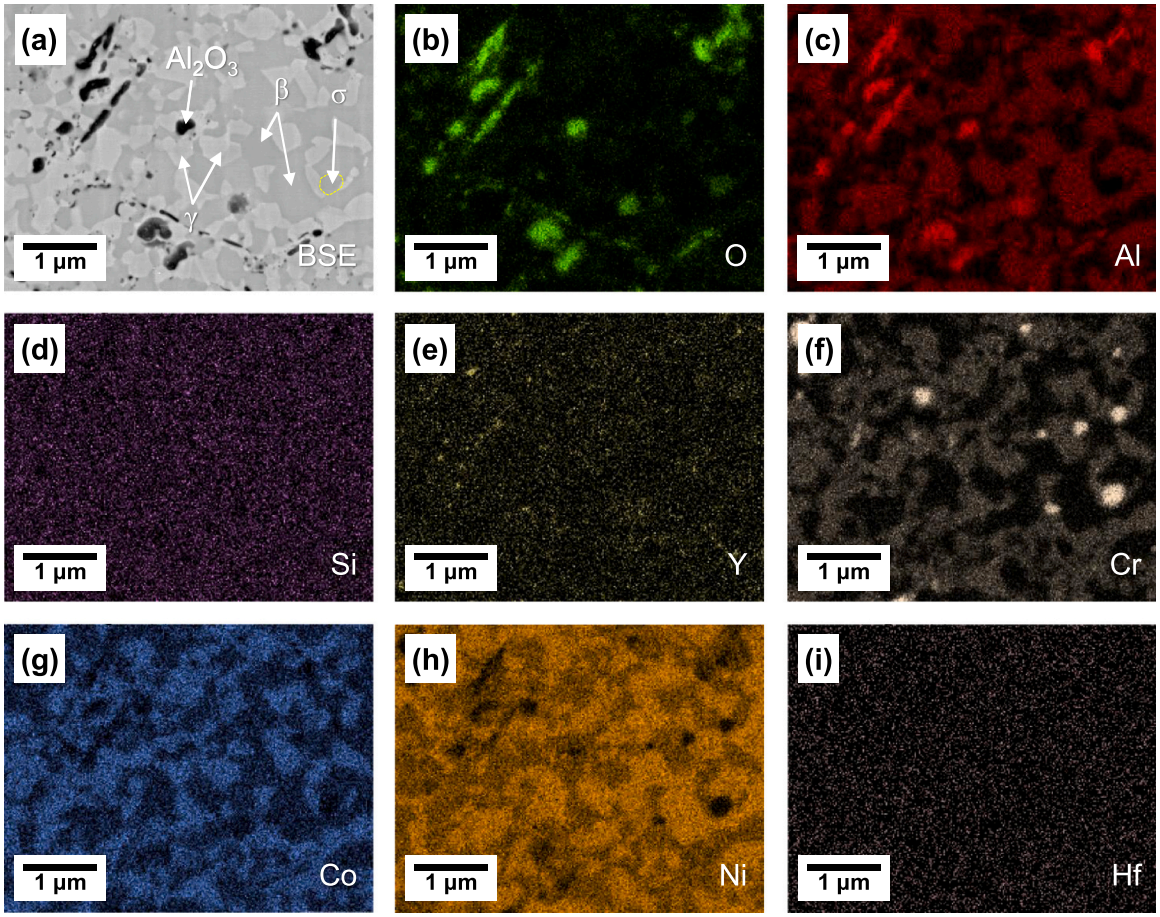

Fig. 4. (a) SEM-BSE image of the NiCoCrAlYHfSi bond coat before cyclic oxidation tests. The elemental maps analyzed by EDX for (b) O, (c) Al, (d) Si, (e) Y, (f) Cr, (g) Co, (h) Ni, and (i) Hf.

4. Results and discussions

4.1. Cyclic oxidation tests

Fig. 2 shows the number of cycles to failure in the cyclic oxidation tests. The number of cycles to failure is defined as the point at which the TBC has spalled over 30 % of its surface area. The NiCoCrAlYHfSi sample indicated more than twice higher spallation life than the NiCoCrAlY sample. Fig. 3 shows cross-sectional SEM-BSE images of TBC samples before cyclic oxidation tests. The thicknesses of both the top and bond coats, formed by thermal spray, were nearly identical. The bond coat of the NiCoCrAlYHfSi sample contains slightly more oxide particles (dark spots in SEM-BSE image) than that of the NiCoCrAlY. Fig. 4 shows the EDX analysis results of NiCoCrAlYHfSi bond coat. Only O and Al are strongly detected at the oxide position, which indicated that the oxide mainly consisted of Al_2O_3. The variations in the microstructures of the two bond coats are likely due to differences in the particle size distribution of the powder used in the HVOF process. Generally, an increase in oxide in the bond coat is considered undesirable because it leads to a decrease in the concentration of Al in the metallic phase. However, no adverse effects were observed in this study. Another perspective, the presence of oxide in the bond coat might affected the physical properties of the bond coat. However, the volume fraction of oxides was approximately only 5 %. Therefore, it was presumed that oxides did not have a significant effect on the lifetime of the TBC.

Fig. 4 also shows that the microstructure of the bond coat. The bond

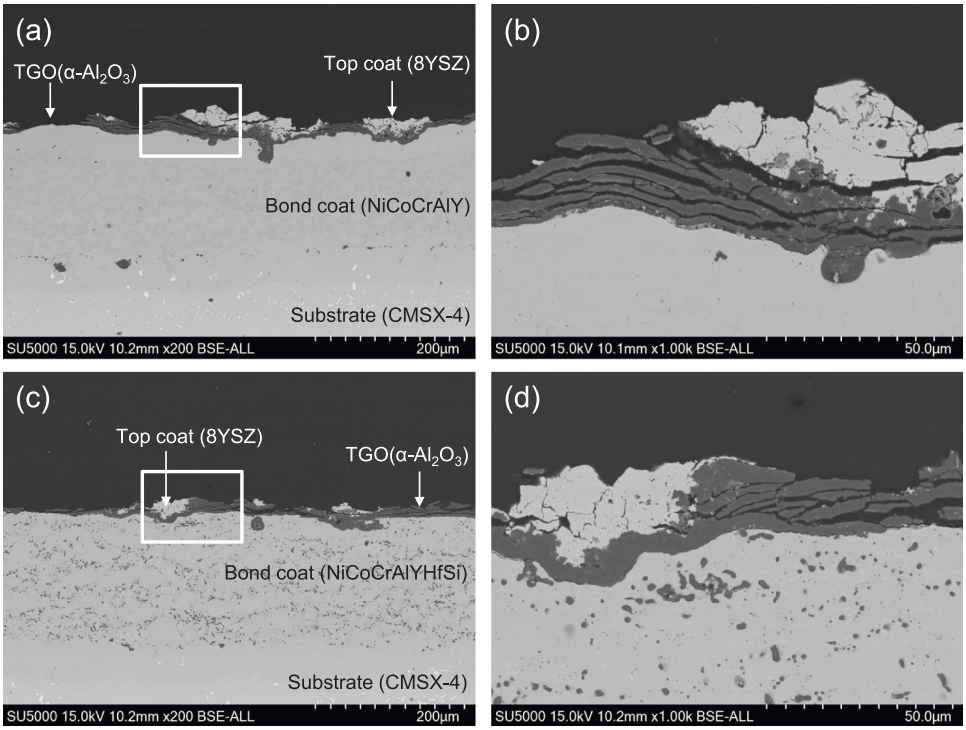

Fig. 5. Cross-section SEM-BSE images of TBC samples after spalling of the top coat by cyclic oxidation tests of 30 min cycles at 1100℃. (a) NiCoCrAlY bond coat sample, the rectangular area in (a) was magnified for (b). NiCoCrAlYHfSi bond coat sample, the rectangular area in (c) was magnified for (d).

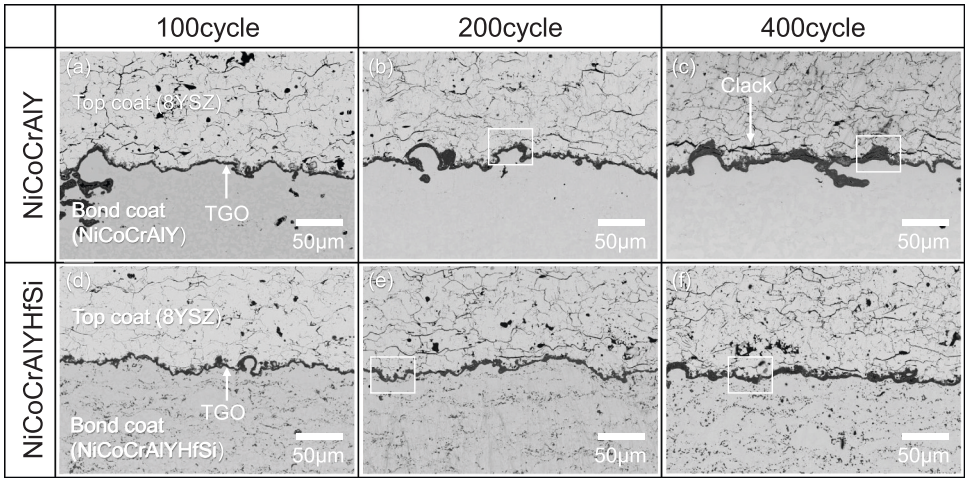

Fig. 6. Cross-section SEM-BSE images of TBC samples after cyclic oxidation tests of 30 min cycles at 1100 ℃. (a) NiCoCrAlY bond coat after 100 cycles, (b) NiCoCrAlY bond coat after 200 cycles, (c) NiCoCrAlY bond coat after 400 cycles, (d) NiCoCrAlYHfSi bond coat after 100 cycles, (e) NiCoCrAlYHfSi bond coat after 200 cycles, (f) NiCoCrAlYHfSi bond coat after 400 cycles.

coat consisted mainly of β-NiAl and γ-Ni phases, with a slight σ-(Co, Cr) phase[43].

The surface roughness of NiCoCrAlY bond coat was Ra = 7.2 μm and that of NiCoCrAlYHfSi bond coat was Ra = 5.3 μm. Although the increase in bond coat roughness is recognized to have a positive effect on the lifetime of TBC[44], the opposite result of cyclic oxidation was obtained. This fact suggests that factors other than surface roughness should have improved the lifetime of the NiCoCrAlYHfSi samples.

Cross-sectional images of the samples after spalling are shown in Fig. 5. Almost no top coat remained after spalling, which indicated that delamination occurred at the interface between the top coat and bond coat. In most areas, the TGO remained on the bond coat, but the TGO was lost in some areas. At several locations, horizontal cracks in the TGO or multi-layered TGO were observed. These features at the surface after spalling were common to the two types of TBC samples, and no clear difference between NiCoCrAlY and NiCoCrAlYHfSi samples was observed.

The cross-sectional microstructures of the samples observed after the cyclic oxidation tests interrupted before spalling are shown in Fig. 6. Fig. 7 are magnified images of the TGO formed in each sample after 200 and 400 cycles of Fig. 6. First, we focused on the growth behavior of the TGO. As shown in Fig. 6, the thickness of the TGO increased as the number of cycles increases. Fig. 8 shows the change in the TGO thickness versus the number of cycles measured from the cross-sectional SEM-BSE images. There was no difference in the TGO thickness between NiCoCrAlY and NiCoCrAlYHfSi samples up to 200 cycles. Specifically, the

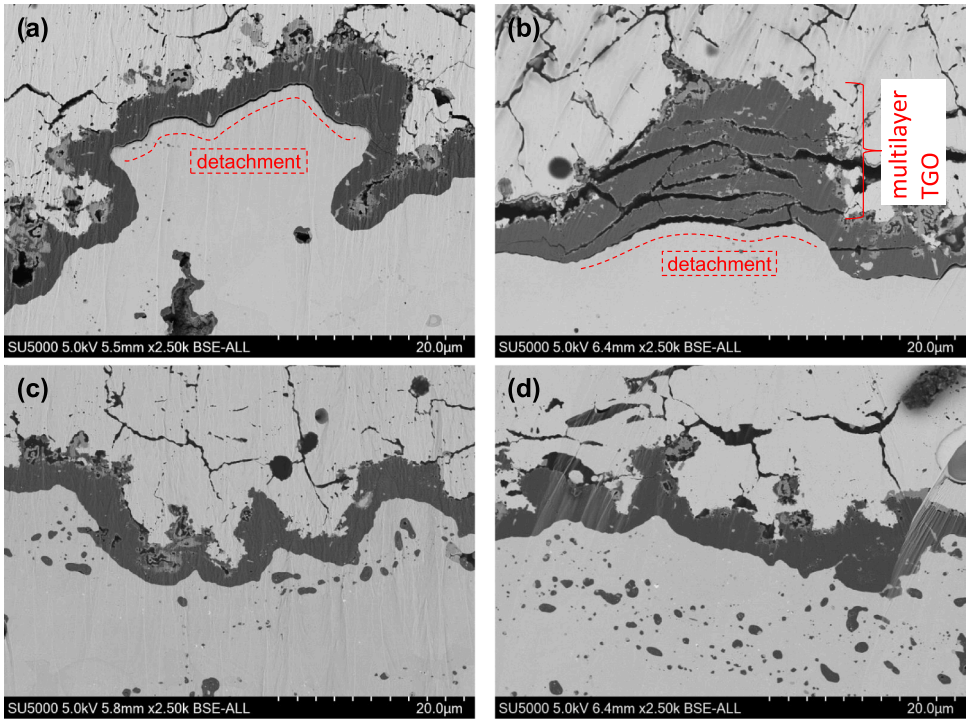

Fig. 7. Cross-section SEM-BSE images of TBC samples after cyclic oxidation tests of 30 min cycles at 1100 ℃. (Blow up views of the white rectangular areas of Fig. 6) (a) NiCoCrAlY bond coat after 200 cycles, (a) NiCoCrAlY bond coat after 400 cycles, (c) NiCoCrAlYHfSi bond coat after 200 cycles, (d) NiCoCrAlYHfSi bond coat after 400 cycles.

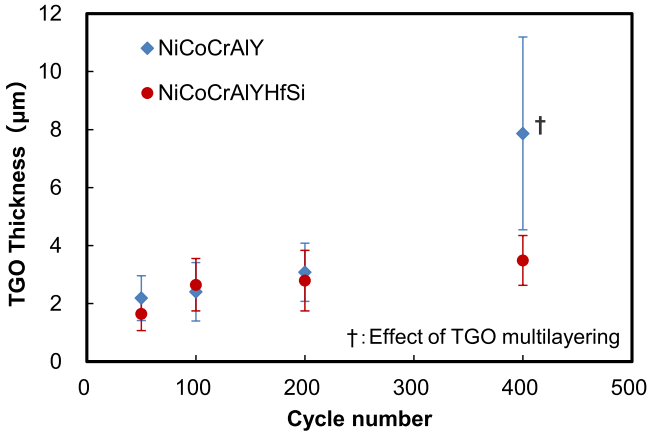

Fig. 8. Thickness of the TGO during cyclic oxidation tests of 30 min cycles at 1100 ℃.

additional doping of Hf and Si did not affect the TGO growth rate. (Although the TGO thickness of NiCoCrAlY increased significantly at 400 cycles, this increase was owing to the formation of the multilayered TGO described later and was not owing to a change of the TGO growth rate itself.) Note that, it has been demonstrated that the RE can affect the growth rate of the TGO in previous studies [14,45–47]. However, in this experiment, the difference of doped RE between the two samples, Y only or YHfSi, does not affect the TGO growth rate. Therefore, the difference in TBC lifetime could not be attributed to the TGO growth rate.

In Fig. 6a, c, internal TGO which formed in the open porosity near the interface was observed. However, the number of such defects is few and limited, and these defects were not considered to have a noticeable effect on TBC lifetime.

We focused on crack initiation and propagation behavior. No obvious crack initiation was observed in either NiCoCrAlY or NiCoCrAlYHfSi samples up to 200 cycles (Fig. 6b, e). However, the magnified TGO image of the NiCoCrAlY sample indicated the TGO had partially detached from the bond coat after 200 cycles (Fig. 7a). In contrast, in the NiCoCrAlYHfSi sample, the TGO had close contact with the bond coat at 200 cycles (Fig. 7c).

At 400 cycles, cracks penetrating through the TGO and the top coat were observed in the NiCoCrAlY sample (Fig. 6c). However, such a large clack was not observed in the NiCoCrAlYHfSi sample (Fig. 6f). Furthermore, in the NiCoCrAlY sample, multilayered TGO was observed everywhere, as shown in Fig. 7b. Such multilayered TGO are considered to have formed by the following process, shown in Fig. 9. First, the TGO is locally detached from the bond coat. Second, under the detached areas, new TGO start to grow. The repetition of such detachment and re-

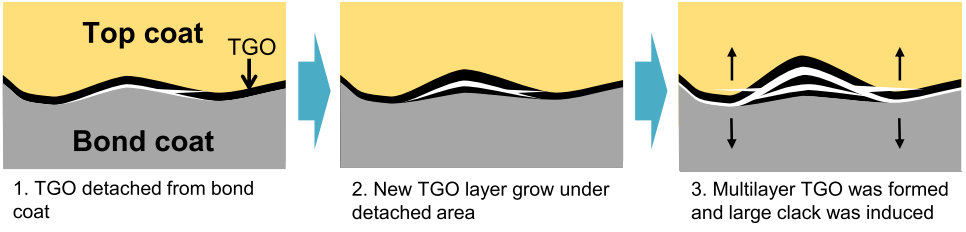

Fig. 9. Schematic illustration showing the mechanisms of the multilayer TGO formation and of the TBC spalling.

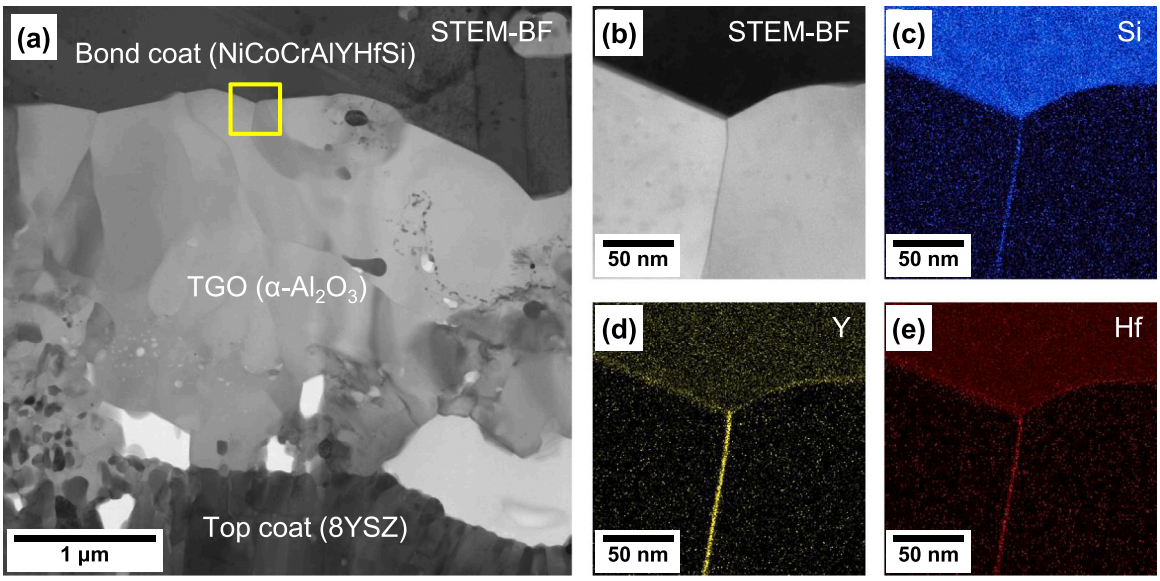

Fig. 10. (a) STEM bright field image of the TGO of the NiCoCrAlYHfSi sample after cyclic oxidation tests of 30 min cycles at 1100 °C for 200 cycles. The rectangular area in (a) was magnified for (b) and analyzed by EDX and elemental maps for (c) Si, (d) Y, and (e) Hf.

growth of the TGO resulted in localized multilayering of the TGO [15, 48,49]. Such localized and significant TGO growth seems to induce out-of-plane stress in the surrounding area, leading to eventual top coat spallation. In particular, cracks that propagated into the top coat occurred around the multilayer TGO (Fig. 6c). Compared to the NiCoCrAlY sample, there were fewer multilayer TGO, and the TGO adhered to the bond coat in the NiCoCrAlYHfSi sample at 400 cycles, as shown in Figs. 6f and 6d.

Note that no oxide "peg" formation was observed at the interface between the TGO and the bond coat in any samples in this study. The formation of oxide peg consisting of RE-oxide is a well-known mechanism that improves the TGO adhesion [21]. Therefore, the adhesion of TGO in NiCoCrAlYHfSi samples was improved despite the absence of oxide peg, and additional RE (Si, Hf) doping might increase the adhesion strength of TGO by another mechanism.

Furthermore, in Fig. 7, "gray" oxides were observed between the α-Al_2O_3 TGO and the top coat. Based on the results of our previous study [38], which investigated oxidation behavior after pre-oxidation, these oxides seemed to be Cr_2O_3. Cr_2O_3 forms in the early stage of oxidation, so its effect on the TBC lifetime should be limited. Moreover, no difference in the state of Cr_2O_3 formation was observed between the NiCoCrAlY and NiCoCrAlYHfSi samples.

Fig. 10a shows the cross-sectional STEM image of the TGO formed in the NiCoCrAlYHfSi sample after 200 cycles. The TGO has the typical columnar α-Al_2O_3 microstructure, as reported in the previous research [26]. The magnified image of the interface between the bond coat and the TGO as well as the elemental map of Si, Y, and Hf by EDX are shown in Fig. 10b-e. Si, Y, and Hf maps show segregation on oxide grain boundaries (Fig. 10c-e). In addition, Y and Hf segregated slightly at the oxide-metal interface (Fig. 10d, e). This RE segregation at the interface may have affected the adhesion of the TGO.

To summarize the experimental results, the additional doping of Hf and Si for the NiCoCrAlYHfSi samples improved the adhesion of the TGO to the bond coat, and the improvement avoided the formation of multilayer TGO. Consequently, the lifetime of the TBC samples should be improved.

4.2. DFT calculations

4.2.1. Segregation stability of RE

To determine the favorable occupation site of the RE atom at the interface between α-Al_2O_3(0001) and γ-Ni(111), we calculated segregation energy. The segregation energy E^i_{seg} is defined as follows.

$$E^i_{seg} = E_{X,\,i} - \quad E_{X,\,H} \tag{6}$$

Where $E_{X,i}$ and $E_{X,H}$ are the total energies when RE atom X replaces a Al atom at i site and H site (shown in Fig. 11b), respectively. Because H site

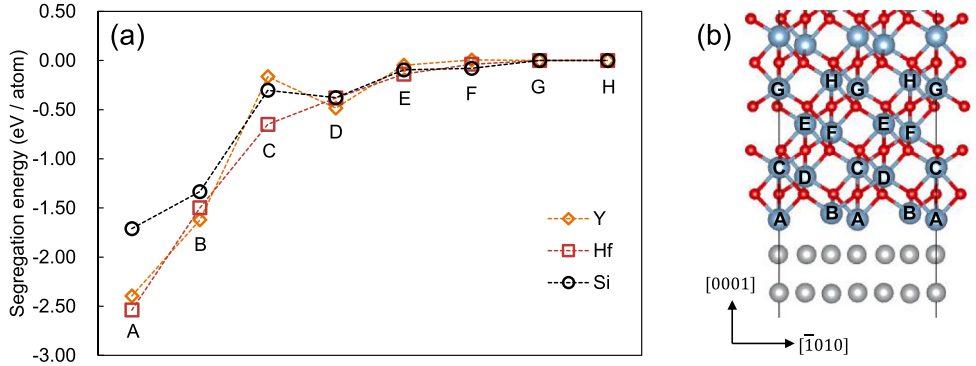

Fig. 11. (a) Relationship between segregation energies and the RE atom distribution. Alphabetical characters indicate the site where an Al atom is replaced with a RE atom. (b) Schematic illustration that indicates assigning letters for Al atom position near the interface.

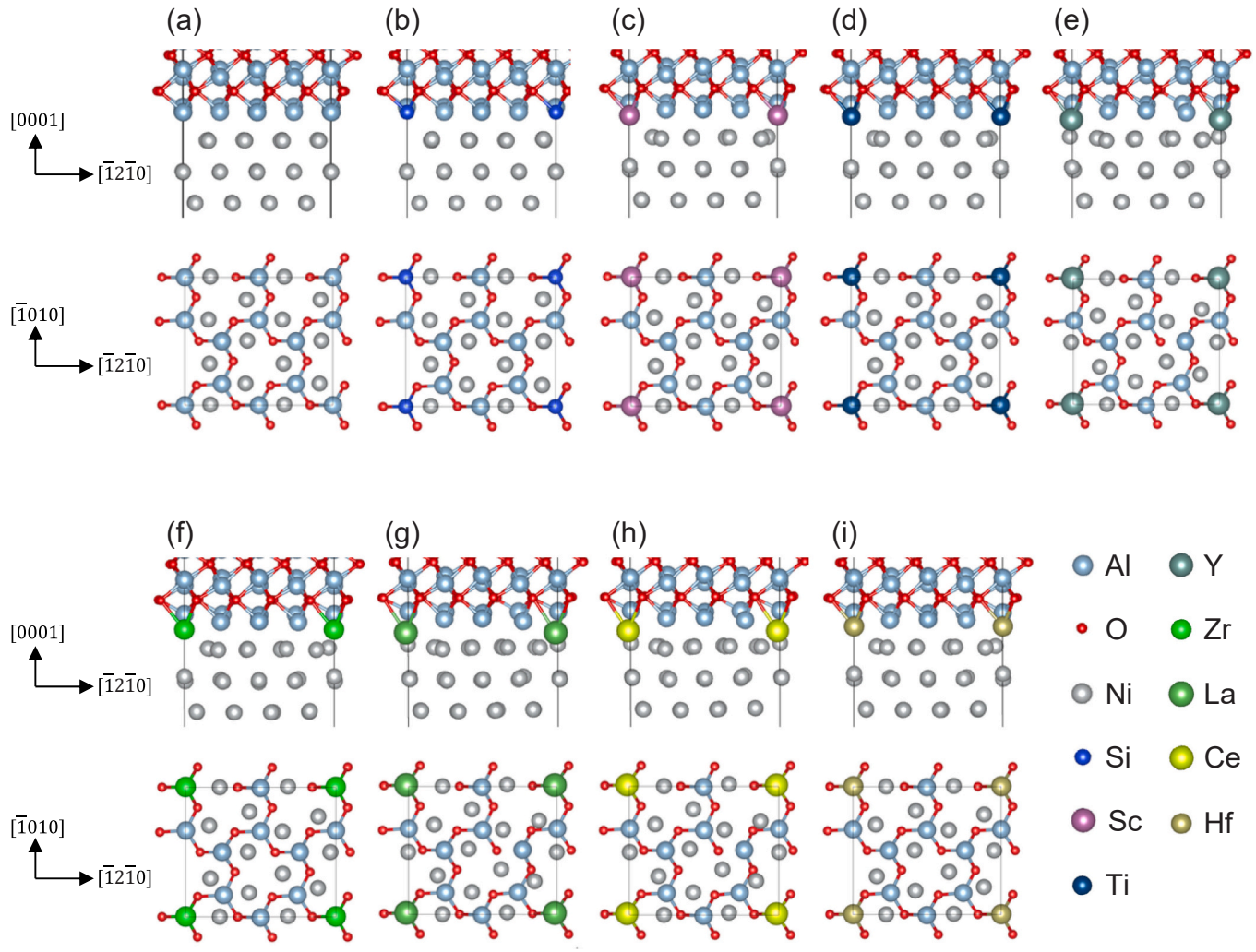

Fig. 12. Optimized structure of the α-Al_2O_3/γ-Ni interfaces. (a) clean interface, (b) Si-doped, (c) Sc-doped, (d) Ti-doped, (e) Y-doped, (f) Zr-doped, (g) La-doped, (h) Ce-doped, (i) Hf-doped.

is the furthest from either of the two interfaces, (shown in Fig. 1) we considered that the doping RE to H site is equivalent to the doping to the bulk α-Al_2O_3. A negative value of E^i_{seg} indicates that it is more favorable for the doped-RE to occupy that site. The variation of E^i_{seg} as a function of RE position in the 118-atoms size model is shown in Fig. 11a. The segregation energy decreases when RE atoms are doped closer to the interface, which is lowest at site A, closest to the interface. Therefore, the RE atoms segregate at the interface. The reason for the segregation of Y and Hf at the oxide-metal interface of NiCoCrAlYHfSi sample, shown in Fig. 10 in Section 4.1, can be explained by this calculation results. This result indicates the possibility of Si segregation, which could not be observed by STEM-EDX analysis.

Although segregation energy was calculated only for three types of RE (Y, Hf, and Si), A site was the most stable for all three RE. Thus, we assumed that the A site would be the most stable site for all other RE atoms, and subsequent calculations were performed with doping RE at only A site.

4.2.2. *Effect of RE-doping for adhesion strength*

The structure of the fully relaxed interface without and with various doped-RE (Si, Sc, Ti, Y, Zr, La, Ce, and Hf) is shown in Fig. 12. In the case of a clean interface (Fig. 12a) and RE with a small ionic radius (such as Si, shown in Fig. 12b), the FCC structures of γ-Ni at the interface are almost completely maintained. The doping of RE, which has a relatively large ionic radius compared to Al, such as Y (Fig. 12e), La (Fig. 12g), and Ce (Fig. 12h), causes changes in Ni-atom position in the lattice around the RE, and the structures of γ-Ni near the interface changed slightly from the ideal FCC structure. However, these changes are limited to the second layer from the interfaces, and the structures of γ-Ni beyond the third layer are preserved as the FCC structure. However, the structure of the α-Al_2O_3 side was almost maintained in all RE-doped models.

The interface energies of RE-doped interfaces are listed in Table 2. It is indicated that all interface energies are decreased by the doping of RE compared to the clean interface. This result suggests that the interface becomes more stable with doped RE and that the bonding strength of the interface should be improved. However, the amount of reduction in interface energy varies significantly depending on the doped RE

Table 2
Interface energies γ of the clean and RE doped α-Al_2O_3/γ-Ni interfaces.

Dopant	Clean	Si	Sc	Ti	Y	Zr	La	Ce	Hf
γ (J/m^2)	2.50	1.62	2.47	2.15	2.31	1.80	2.04	2.15	1.84

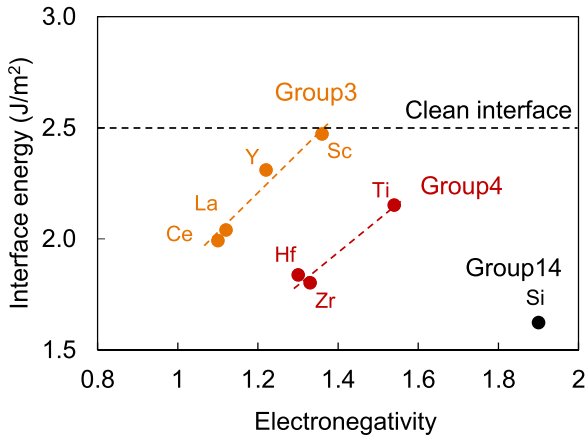

Fig. 13. Interface energies of doped α-Al_2O_3/γ-Ni interface as a function of electronegativity of RE.

elements. The Si-doped interface shows the lowest interface energy value of 1.62 J/m^2, followed by Zr and Hf (1.80 J/m^2 and 1.84 J/m^2, respectively). Y, which is the most common RE, shows a relatively high interface energy of 2.31 J/m^2, which is close to the value of the clean interface (2.50 J/m^2). Some trends, including the greater effect of Hf compared to Y and the fact that there is a slight difference between Hf and Zr doping, are consistent with the previous studies on α-Al_2O_3/β-NiAl [28,30,32].

These calculated results indicating that Si and Hf doping significantly increase the adhesion strength of α-Al_2O_3/γ-Ni compared to Y doping are in good agreement with the differences in lifetime and spalling behavior between NiCoCrAlY and NiCoCrAlYHfSi samples in the experimental results. The agreement between the experimental and analytical results presents strong evidence that Hf and Si improve TGO adhesion and oxidation resistance through their segregation at the interface.

To clarify the trend of the interface energies, we plotted interface energies of the RE-doped interface as a function of Pauling electronegativity [50] of RE as shown in Fig. 13. RE of Group IV elements (Ti, Hf, and Zr) indicate relatively smaller interface energies than that of Group III elements (Sc, Y, La, and Ce). Furthermore, as the electronegativity of RE decreases, interface energies become more negative between RE of the same group (Group III and Group IV), respectively.

To underline the different effects of each RE doping on the interface bonding, the *CD* and the *CDD* are compared in Fig. 14. Focusing on the RE-Ni bond, the *CDD* plots show that the charge density locally increases between doped RE and Ni atoms in all interfaces. This result indicates that the bonding between RE-Ni is covalent. Furthermore, for Si (Fig. 14b) and Group IV elements (Ti (Fig. 14d), Zr (Fig. 14f), and Hf (Fig. 14i)), the degree of charge density localization is stronger than that for Group III elements (Sc (Fig. 14d), Y (Fig. 14e), La (Fig. 14g), and Ce (Fig. 14h)) as shown in *CDD* map. This result suggests that the covalent bonding of RE-Ni of Group IV elements and Si are stronger than those of Group III elements, which may be the reason for the difference in interface energies between Group III and IV elements (shown in Fig. 13).

For a deeper understanding of the electronic origin of chemical bonding at the RE-doped interface needs further investigation of the projected density of states (PDOS). Fig. 15 presents the PDOS of clean and different RE-doped interfaces (Si, Y and Zr). In the clean interface, the Al p-orbital (Fig. 15a) occupies the same energy band as the Ni d-orbital (Fig. 15b). This result indicates the presence of the hybridization between the Al-p and Ni-d states. In the Si-doped interface, the Si p-orbital (Fig. 15c) also occupies the same energy band as the Ni d-orbital (Fig. 15d); however, Si p-orbital at that energy band is larger than Al p-orbital of the clean interface, suggesting the formation of stronger covalent bonding of Si-doped interface. The difference in the number of valence electrons in the p-orbitals (Al: 1, Si: 2) may affect the bonding strength.

Similarly, in the case of Y and Zr doped interface, the Y d- and Zr d-orbitals occupy the same energy bands as the Ni d-orbital, suggesting that covalent bonds are formed by hybridization of the d-orbitals. Furthermore, the DOS at that energy band is higher for the Zr d-orbital than for the Y d-orbital. Therefore, Zr formed a stronger covalent bond

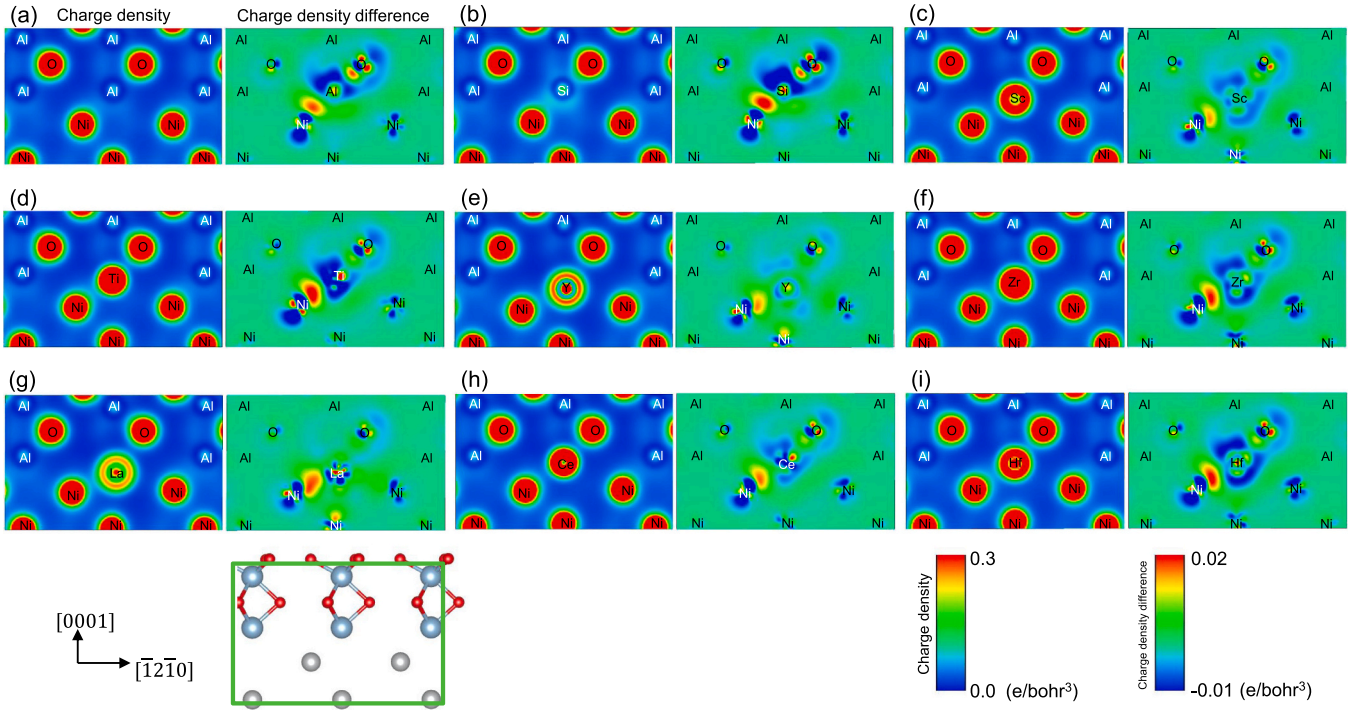

Fig. 14. Charge density and charge density difference for the RE doped α-Al_2O_3/γ-Ni interface. (a) clean interface, (b) Si-doped, (c) Sc-doped, (d) Ti-doped, (e) Y-doped, (f) Zr-doped, (g) La-doped, (h) Ce-doped, (i) Hf-doped.

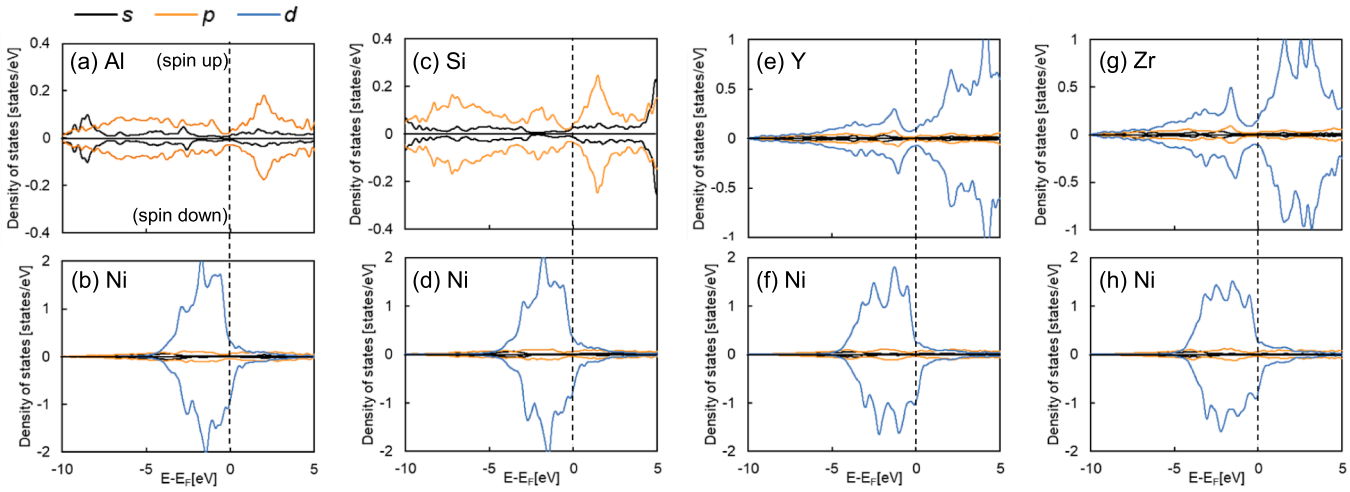

Fig. 15. DOS for the RE doped α-Al_2O_3/γ-Ni interface of (a) Al atom and (b) Ni atom in the clean interface; (c) Si atom and (d) Ni atom of Si-doping; (e) Y atom and (f) Ni atom of Y-doping; (g) Zr atom and (h) Ni atom of Zr-doping.

than Y. As in the case with Si-doping, the difference of valence electrons number in the d-orbitals of RE might affect this difference. The number of valence electrons in the d-orbitals is one for Group III elements (Sc, Y, La, and Ce) and two for Group IV elements (Ti, Zr, Hf). This difference is assumed to affect the strength of the covalent bonding between RE and Ni, resulting in the difference in the interface energies between Group III and IV elements as shown in Fig. 13.

5. Conclusions

In this study, we first conducted cyclic oxidation tests on NiCoCrAlY and NiCoCrAlYHfSi TBC samples to evaluate their durability and understand the effects of the RE difference of the MCrAlX used as the bond coat. The NiCoCrAlYHfSi sample showed better durability than the NiCoCrAlY sample. Cross-sectional observation for each sample revealed that the NiCoCrAlY sample showed relatively poor adhesion of the TGO to the bond coat, causing a difference in the lifetime in the cyclic oxidation tests.

To clarify the effect of RE-doping on TGO adhesion improvement, DFT calculations were performed for the RE-doped α-Al_2O_3(0001)/γ-Ni (111) interface. All doped RE (Si, Sc, Ti, Y, Zr, La, Ce, and Hf) reduced the interface energies; however, the effect was relatively small for Y, while Si and Hf were found to be more effective. This calculation result is consistent with the difference in lifetime between NiCoCrAlY and NiCoCrAlYHfSi samples under cyclic oxidation tests. Furthermore, comparing Group III elements (Sc, Y, La, and Ce) and Group IV elements (Ti, Zr, and Hf), the reduction in interface energies was larger for Group IV than for Group III, and for each group, there was a correlation between the electronegativity of REs and interface energy.

CRediT authorship contribution statement

Ryoji Sahara: Writing – review & editing, Methodology. **Yoko Yamabe-Mitarai:** Writing – review & editing, Supervision. **Masahiro Negami:** Writing – original draft, Visualization, Investigation, Conceptualization. **Ryo Morihashi:** Supervision, Project administration. **Tessei Yoshino:** Investigation.

Declaration of Competing Interest

The authors declare that they have no known competing financial interests or personal relationships that could have appeared to influence the work reported in this paper.

Data availability

Data will be made available on request.

Acknowledgment

We acknowledge Center for Computational Materials Science, Institute for Materials Research, Tohoku University for the use of MASAMUNE-IMR (Project No. 2022120-SCKXX-0506). The authors thank the Supercomputer Center, the Institute for Solid State Physics, the University of Tokyo for the use of the facilities.

Appendix A. Supporting information

Supplementary data associated with this article can be found in the online version at doi:10.1016/j.corsci.2024.112329.

References

[1] J. Nicholls, Advances in coating design for high-performance gas turbines, MRS Bull. 28 (9) (2003) 659–670. https://doi.org/10.1557/mrs2003.194.
[2] N.P. Padture, M. Gell, E.H. Jordan, Materials science - Thermal barrier coatings for gas-turbine engine applications, Science 296 (5566) (2002) 280–284. https://doi.org/10.1126/science.1068609.
[3] Q.Q. Zhou, L. Yang, C. Luo, F.W. Chen, Y.C. Zhou, Y.G. Wei, Thermal barrier coatings failure mechanism during the interfacial oxidation process under the interaction between interface by cohesive zone model and brittle fracture by phase-field, Int. J. Solids Struct. 214 (2021) 18–34. https://doi.org/10.1016/j.ijsolstr.2020.12.020.
[4] W. Zhu, L. Yang, J.W. Guo, Y.C. Zhou, C. Lu, Determination of interfacial adhesion energies of thermal barrier coatings by compression test combined with a cohesive zone finite element model, Int. J. Plast. 64 (2015) 76–87. https://doi.org/10.1016/j.ijplas.2014.08.003.
[5] L. Yang, Q.X. Liu, Y.C. Zhou, W.G. Mao, C. Lu, Finite Element Simulation on Thermal Fatigue of a Turbine Blade with Thermal Barrier Coatings, J. Mater. Sci. Technol. 30 (4) (2014) 371–380. https://doi.org/10.1016/j.jmst.2013.11.005.
[6] L. Yang, Y.C. Zhou, C. Lu, Damage evolution and rupture time prediction in thermal barrier coatings subjected to cyclic heating and cooling: An acoustic emission method, Acta Mater. 59 (17) (2011) 6519–6529. https://doi.org/10.1016/j.actamat.2011.06.018.
[7] Q. Shen, L. Yang, Y.C. Zhou, Y.G. Wei, W. Zhu, Effects of growth stress in finite-deformation thermally grown oxide on failure mechanism of thermal barrier coatings, Mech. Mater. 114 (2017) 228–242. https://doi.org/10.1016/j.mechmat.2017.08.011.
[8] J.L. Smialek, R.A. Miller, Revisiting the Birth of 7YSZ Thermal Barrier Coatings: Stephan Stecura, Coatings 8 (7) (2018) 255. https://doi.org/10.3390/coatings8070255.
[9] C.U. Hardwicke, Y.C. Lau, Advances in Thermal Spray Coatings for Gas Turbines and Energy Generation: A Review, J. Therm. Spray. Technol. 22 (5) (2013) 564–576. https://doi.org/10.1007/s11666-013-9904-0.

[10] F. Ghadami, A.S.R. Aghdam, S. Ghadami, Microstructural characteristics and oxidation behavior of the modified MCrAlX coatings: A critical review, Vacuum 185 (2021) 109980. https://doi.org/10.1016/j.vacuum.2020.109980.
[11] C.G. Levi, J.W. Hutchinson, M.H. Vidal-Sétif, C.A. Johnson, Environmental degradation of thermal-barrier coatings by molten deposits, MRS Bull. 37 (10) (2012) 932–941. https://doi.org/10.1557/mrs.2012.230.
[12] R. Darolia, Thermal barrier coatings technology: critical review, progress update, remaining challenges and prospects, Int. Mater. Rev. 58 (6) (2013) 315–348. https://doi.org/10.1179/1743280413y.0000000019.
[13] Y.C. Zhou, T. Hashida, Coupled effects of temperature gradient and oxidation on thermal stress in thermal barrier coating system, Int. J. Solids Struct. 38 (24–25) (2001) 4235–4264. https://doi.org/10.1016/s0020-7683(00)00309-7.
[14] D. Naumenko, B.A. Pint, W.J. Quadakkers, Current Thoughts on Reactive Element Effects in Alumina-Forming Systems, Memory of John StringerOxid. Met (1–2) (2016) 1–43. https://doi.org/10.1007/s11085-016-9625-0.
[15] J.A. Haynes, K.A. Unocic, B.A. Pint, Effect of water vapor on the 1100 °C oxidation behavior of plasma-sprayed TBCs with HVOF NiCoCrAlX bond coatings, Surf. Coat. Technol. 215 (2013) 39–45. https://doi.org/10.1016/j.surfcoat.2012.07.099.
[16] K. Fritscher, The Reactive Element Effect, Metall. Mater. Trans. A 54 (2023) 64–74. https://doi.org/10.1007/s11661-022-06840-w.
[17] W.H. Duan, Y.L. Li, W.J. Qiang, Effect of Hf-Doped MCrAlY Alloy on the Structure and Properties of Thermally Grown Oxide Layer, J. Mater. Eng. Perform. (2023). https://doi.org/10.1007/s11665-023-08657-z.
[18] W.T. Griffiths, L.B. Pfeil, Improvements in Heat Resistant Alloys, U. K., 1937, Patent No. 459848.
[19] L.B. Pfeil, Improvements Relating to Heat Resisting Alloys Containing Chromium, U.K., 1945, Patent No. 574088.
[20] D.K. Gupta, D.S. Duvall, A silicon and hafnium modified plasma sprayed MCrAlY coating for single crystal superalloys, in: W.B.K.R.H. Bricknell, M. Gell, C. S. Kortovich, J.F. Radavich (Eds.), Superalloys 1984, The Metallurgical Society of AIME, Warrendale, 1984, pp. 711–720.
[21] H. Hindam, D.P. Whittle, Peg Formation by Short-Circuit Diffusion in Al_2O_3 Scales Containing Oxide Dispersions, J. Electrochem. Soc. 129 (5) (1982) 1147–1149. https://doi.org/10.1149/1.2124044.
[22] A.W. Funkenbusch, J.G. Smeggil, N.S. Bornstein, Reactive element-sulfur interaction and oxide scale adherence, Metall. Trans. A 16 (6) (1985) 1164–1166. https://doi.org/10.1007/BF02811687.
[23] B.G. Mendis, K.J.T. Livi, K.J. Hemker, Observations of reactive element gettering of sulfur in thermally grown oxide pegs, Scr. Mater. 55 (7) (2006) 589–592. https://doi.org/10.1016/j.scriptamat.2006.06.017.
[24] E. Schumann, J.C. Yang, M.J. Graham, M. Ruhle, Segregation studies of oxidized Y and Zr doped NiAl, Werkst, Und Korros. -Mater. Corros. 46 (4) (1995) 218–222. https://doi.org/10.1002/maco.19950460405.
[25] K.A. Unocic, Y.M. Chen, D.W. Shin, B.A. Pint, E.A. Marquis, STEM and APT characterization of scale formation on a La,Hf,Ti-doped NiCrAl model alloy, Micron 109 (2018) 41–52. https://doi.org/10.1016/j.micron.2018.01.011.
[26] B.A. Pint, K.L. More, Characterization of alumina interfaces in TBC systems, J. Mater. Sci. 44 (7) (2009) 1676–1686. https://doi.org/10.1007/s10853-008-3221-x.
[27] E.A.A. Jarvis, E.A. Carter, An atomic perspective of a doped metal-oxide interface, J. Phys. Chem. B 106 (33) (2002) 7995–8004. https://doi.org/10.1021/jp0257348.
[28] I. Ozfidan, K.Y. Chen, M. Fu, Effects of Additives and Impurity on the Adhesive Behavior of the NiAl(110)/Al_2O_3 (0001) Interface: An Ab Initio Study, Metall. Mater. Trans. A 42 (13) (2011) 4126–4136. https://doi.org/10.1007/s11661-011-0813-x.
[29] Y. Jiang, J.R. Smith, A.G. Evans, First principles assessment of metal/oxide interface adhesion, Appl. Phys. Lett. 92 (14) (2008). https://doi.org/10.1063/1.2907339.
[30] Z. Zhang, R.F. Zhang, D. Legut, D.Q. Li, S.H. Zhang, Z.H. Fu, H.B. Guo, Pinning effect of reactive elements on adhesion energy and adhesive strength of incoherent Al_2O_3/NiAl interface, Phys. Chem. Chem. Phys. 18 (33) (2016) 22864–22873. https://doi.org/10.1039/c6cp03609k.
[31] E.A. Jarvis, E.A. Carter, The role of reactive elements in thermal barrier coatings, Comput. Sci. Eng. 4 (2) (2002) 33–41. https://doi.org/10.1109/5992.988645.
[32] Z. Zhang, C.C. Hu, H. Chen, J. He, Pinning effect of reactive elements on structural stability and adhesive strength of environmental sulfur segregation on Al_2O_3/NiAl interface, Scr. Mater. 188 (2020) 174–178. https://doi.org/10.1016/j.scriptamat.2020.07.038.
[33] M. Negami, S. Hibino, A. Kawano, Y. Nomura, R. Tanaka, K. Igashira, Development of Highly Durable Thermal Barrier Coating by Suppression of Thermally Grown Oxide, J. Eng. Gas. Turbines Power 140 (8) (2018) 082101. https://doi.org/10.1115/1.4038607.
[34] ISO, Metallic and other inorganic coatings - Test methods for measuring thermal cycle resistance and thermal shock resistance for thermal barrier coatings; ISO 14188:2012.
[35] P. Giannozzi, S. Baroni, N. Bonini, M. Calandra, R. Car, C. Cavazzoni, D. Ceresoli, G.L. Chiarotti, M. Cococcioni, I. Dabo, A. Dal Corso, S. de Gironcoli, S. Fabris, G. Fratesi, R. Gebauer, U. Gerstmann, C. Gougoussis, A. Kokalj, M. Lazzeri, L. Martin-Samos, N. Marzari, F. Mauri, R. Mazzarello, S. Paolini, A. Pasquarello, L. Paulatto, C. Sbraccia, S. Scandolo, G. Sclauzero, A.P. Seitsonen, A. Smogunov, P. Umari, R.M. Wentzcovitch, QUANTUM ESPRESSO: a modular and open-source software project for quantum simulations of materials, J. Phys.: Condens. Matter 21 (39) (2009) 395502. https://doi.org/10.1088/0953-8984/21/39/395502.
[36] P.E. Blochl, Projector augmented-wave method, Phys. Rev. B 50 (24) (1994) 17953–17979. https://doi.org/10.1103/PhysRevB.50.17953.
[37] J.P. Perdew, K. Burke, M. Ernzerhof, Generalized gradient approximation made simple, Phys. Rev. Lett. 77 (18) (1996) 3865–3868. https://doi.org/10.1103/PhysRevLett.78.1396.
[38] M. Negami, K. Kyuma, M. Azuma, T. Taniguchi, Y. Yamabe-Mitarai, Improvement of the durability of thermal barrier coating by pre-oxidation, Corros. Sci. 227 (2024) 111806. https://doi.org/10.1016/j.corsci.2023.111806.
[39] Y. Chen, P. Xiao, Micromechanical testing of a thermally grown oxide on a MCrAlY coating Surf, Coat. Technol. 419 (2021), https://doi.org/10.1016/j.surfcoat.2021.127300.
[40] E.A.A. Jarvis, A. Christensen, E.A. Carter, Weak bonding of alumina coatings on Ni (111), Surf, Surf. Sci. 487 (1–3) (2001) 55–76, https://doi.org/10.1016/S0039-6028(01)01071-8.
[41] J. Bandyopadhyay, K.P. Gupta, Low temperature lattice parameter of nickel and some nickel-cobalt alloys and Grüneisen parameter of nickel, Cryogenics 17 (6) (1977) 345–347. https://doi.org/10.1016/0011-2275(77)90130-8.
[42] M. Lucht, M. Lerche, H.C. Wille, Y.V. Shvyd'ko, H.D. Rüter, E. Gerdau, P. Becker, Precise measurement of the lattice parameters of α-Al_2O_3 in the temperature range 4.5–250 K using the Mossbauer wavelength standard, J. Appl. Crystallogr. 36 (2003) 1075–1081. https://doi.org/10.1107/s0021889803011051.
[43] D.R.G Achar, R. Munoz-Arroyo, L. Singheiser, W.J. Quadakkers, Modelling of phase equilibria in MCrAlY coating systems, Surf, Coat. Technol. 187 (2–3) (2004) 272–283, https://doi.org/10.1016/j.surfcoat.2004.02.018.
[44] W. Nowak, D. Naumenko, G. Mor, F. Mor, D.E. Mack, R. Vassen, L. Singheiser, W. J. Quadakkers, Effect of processing parameters on MCrAlY bondcoat roughness and lifetime of APS-TBC systems, Surf. Coat. Technol. 260 (2014) 82–89. https://doi.org/10.1016/j.surfcoat.2014.06.075.
[45] B.A. Pint, Optimization of reactive-element additions to improve oxidation performance of alumina-forming alloys, J. Am. Ceram. Soc. 86 (4) (2003) 686–695. https://doi.org/10.1111/j.1151-2916.2003.tb03358.x.
[46] T. Matsudaira, M. Wada, T. Saitoh, S. Kitaoka, Oxygen permeability in cation-doped polycrystalline alumina under oxygen potential gradients at high temperatures, Acta Mater. 59 (14) (2011) 5440–5450. https://doi.org/10.1016/j.actamat.2011.05.018.
[47] J. He, Z. Zhang, H. Peng, S.K. Gong, H.B. Guo, The role of Dy and Hf doping on oxidation behavior of two-phase ($\gamma' + \beta$) Ni-Al alloys, Corros. Sci. 98 (2015) 699–707. https://doi.org/10.1016/j.corsci.2015.06.016.
[48] J.A. Haynes, M.K. Ferber, W.D. Porter, E.D. Rigney, Characterization of alumina scales formed during isothermal and cyclic oxidation of plasma-sprayed TBC systems at 1150°C, Oxid. Met. 52 (1–2) (1999) 31–76, https://doi.org/10.1023/a:1018870923397.
[49] D. Naumenko, V. Shemet, L. Singheiser, W.J. Quadakkers, Failure mechanisms of thermal barrier coatings on MCrAlY-type bondcoats associated with the formation of the thermally grown oxide, J. Mater. Sci. 44 (7) (2009) 1687–1703. https://doi.org/10.1007/s10853-009-3284-3.
[50] J.E. Huheey, E.A. Keiter, R.L. Keiter, Inorganic Chemistry - principles of structure and reactivity, 4th ed., Hapere Collins, New York, 1993.